

High-Frequency Radar Mapping of Surface Currents Using WERA

LYNN K. SHAY, JORGE MARTINEZ-PEDRAJA, THOMAS M. COOK,* AND BRIAN K. HAUS

Rosenstiel School of Marine and Atmospheric Science, University of Miami, Miami, Florida

ROBERT H. WEISBERG

Department of Marine Science, University of South Florida, St. Petersburg, Florida

(Manuscript received 26 September 2005, in final form 12 June 2006)

ABSTRACT

A dual-station high-frequency Wellen Radar (WERA), transmitting at 16.045 MHz, was deployed along the west Florida shelf in phased array mode during the summer of 2003. A 33-day, continuous time series of radial and vector surface current fields was acquired starting on 23 August ending 25 September 2003. Over a 30-min sample interval, WERA mapped coastal ocean currents over an ≈ 40 km \times 80 km footprint with a 1.2-km horizontal resolution. A total of 1628 snapshots of the vector surface currents was acquired, with only 70 samples (4.3%) missing from the vector time series. Comparisons to subsurface measurements from two moored acoustic Doppler current profilers revealed RMS differences of 1 to 5 cm s⁻¹ for both radial and Cartesian current components. Regression analyses indicated slopes close to unity with small biases between surface and subsurface measurements at 4-m depth in the east–west (u) and north–south (v) components, respectively. Vector correlation coefficients were 0.9 with complex phases of -3° and 5° at EC4 (20-m isobath) and NA2 (25-m isobath) moorings, respectively.

Complex surface circulation patterns were observed that included tidal and wind-driven currents over the west Florida shelf. Tidal current amplitudes were 4 to 5 cm s⁻¹ for the diurnal and semidiurnal constituents. Vertical structure of these tidal currents indicated that the semidiurnal components were predominantly barotropic whereas diurnal tidal currents had more of a baroclinic component. Tidal currents were removed from the observed current time series and were compared to the 10-m adjusted winds at a surface mooring. Based on these time series comparisons, regression slopes were 0.02 to 0.03 in the east–west and north–south directions, respectively. During Tropical Storm Henri's passage on 5 September 2003, cyclonically rotating surface winds forced surface velocities of more than 35 cm s⁻¹ as Henri made landfall north of Tampa Bay, Florida. These results suggest that the WERA measured the surface velocity well under weak to tropical storm wind conditions.

1. Introduction

Ocean surface current measurements have been one of the more elusive challenges to confront ocean scientists. Given increased national attention on the coastal ocean and in the planned networking of coastal ocean

observatories, the acquisition of high quality surface current data is required to provide spatial context for emerging suites of in situ instrumentation and the national coastal ocean backbone. The Doppler radar technique has steadily evolved over the past five decades based on the pioneering work of Crombie (1955). Radar signals are backscattered from the moving ocean surface by resonant surface waves of one-half the incident radar wavelength. This Bragg scattering effect results in two discrete peaks in the Doppler spectrum (Stewart and Joy 1974). In the absence of a surface current, spectral peaks are symmetric about the Bragg frequency (ν_b) offset from the origin by an amount proportional to $2c_o\lambda^{-1}$, where c_o represents the linear phase speed of the surface wave and λ is the radar wavelength. If there is an underlying surface current, Bragg peaks in the Doppler spectra are displaced by an

* Current affiliation: Marine Physical Laboratory, Scripps Institution of Oceanography, University of California, San Diego, La Jolla, California.

Corresponding author address: Lynn K. Shay, Meteorology and Physical Oceanography Division, Rosenstiel School of Marine and Atmospheric Science, University of Miami, 4600 Rickenbacker Causeway, Miami, FL 33149-1098.
E-mail: nshay@rsmas.miami.edu

amount of $\Delta v = 2V_{cr}\lambda^{-1}$, where V_{cr} is the radial current component along the radar's look direction. To resolve the two-dimensional current fields, at least two radar stations are required where their separation determines the domain of the mapped region. Measurement accuracy for a vector current is a maximum for an angle of intersection of 90° between the two radial beams emanating from each of the radar sites (Chapman et al. 1997). This error in resolving the current vectors increases as the intersection angle departs from this optimal value.

The concept of using high frequency (HF) and very high frequency (VHF) radar pulses to probe ocean surface currents has received considerable attention in coastal oceanographic experiments in Europe and the United States. Two systems that have been used primarily in these experiments are Coastal Ocean Dynamics Applications Radar (CODAR) (Barrick 1992; Paduan and Rosenfeld 1996) and the Ocean Surface Current Radar (OSCR) (Prandle 1987; Shay et al. 1995). More recently, a Weller Radar (WERA) system has been developed that has the flexibility of both beam-forming (BF) and direction-finding (DF) techniques (Gurgel et al. 1999a). In general, however, current direction resolution is more sensitive to beam patterns in DF than in BF algorithms (Lipa and Barrick 1983; Gurgel et al. 1999a,b).

Previous comparisons of HF-radar-derived currents to in situ measurements have been generally limited to tidal bands due in part to their large horizontal scales and well-defined periods (Prandle 1987; Paduan and Rosenfeld 1996). A series of coastal experiments have compared subsurface vector currents using measurements from both fixed and moving platforms to surface currents from HF (Prandle 1987; Shay et al. 1995, 1998a,b; Essen et al. 2000) and VHF (Balsley et al. 1987; Shay et al. 2002, 2003) radars. An important emerging issue in these comparisons is related to range and bandwidth, which sets the horizontal resolution. For long-range HF systems using low frequencies (<10 MHz), bandwidth is a premium, which causes the surface velocity measurement to be integrated over 36–144-km² areas. Depending on the available bandwidth, a point measurement from a mooring centered in a cell may not represent the area (resolution) the HF radar is sampling particularly if the region has high lateral surface current shear. By contrast, for HF (12–30 MHz) and VHF (30–50 MHz) frequencies, bandwidth is usually available to resolve horizontal structure over 1-km² areas or less.

Over 1-km² areas, point-by-point comparisons have revealed both similarities and differences between surface and subsurface current signals (Shay et al. 1998a,b,

2001; Chapman et al. 1997; Emery et al. 2004). Depending on the depth of the subsurface current measurement and the venue, RMS differences have varied between 7 and 23 cm s⁻¹. During the Duck94 experiment, comparisons to a Vector Measuring Current Meter (VMCM) at 4-m depth indicated an RMS difference of 7 cm s⁻¹ over a range of 1 m s⁻¹ from a 29-day time series. Given the VMCM's measurement accuracy of ≈ 2 cm s⁻¹ (Weller and Davis 1980), the accuracy for the surface current measurement was about 5 cm s⁻¹. Although differences still remain, radar-derived surface current measurements represent the integrated currents in the top meter (or less) of the water column ($\lambda/8\pi$) (Stewart and Joy 1974) where winds and waves impact surface currents and near-surface current shears (Graber et al. 1997; Shay et al. 2003). Essen et al. (2000) compared surface currents from both CODAR and WERA instruments to moored subsurface currents from an S4 current meter. RMS differences between CODAR and a 12-element WERA were 9 to 11 cm s⁻¹. Measurements indicated that RMS differences between WERA and an S4 current meter were ≈ 2 cm s⁻¹ less than the RMS difference between CODAR and the S4. Essen and colleagues reported 23 cm s⁻¹ RMS differences on WERA comparisons to a near-bottom mounted current meter at 22-m depth since near-surface comparisons were not possible because a moored ADCP failed during the experiment. The objective here is to assess WERA performance in a regime where moored ADCPs were deployed as part of the University of South Florida's (USF) Coastal Ocean Monitoring and Prediction System (COMPS; Weisberg et al. 2002). These ADCPs provide near-surface velocity measurements at 4-m depth to quantitatively assess WERA's performance in mapping surface radial and velocity fields.

In the following article, surface current observations acquired over the west Florida shelf (WFS) from a WERA HF radar are described and compared to inner-shelf moorings at the 20- and 25-m isobaths. This comparison includes radial currents from both mooring sites following the Emery et al. (2004) approach as well as the Cartesian current components. In addition to barotropic and baroclinic tidal influences (He and Weisberg 2002a), intermittent Loop Current intrusions (He and Weisberg 2003; Weisberg and He 2003), surface winds force upwelling zones along the WFS including southwest of Tampa, Florida, along the 25-m isobaths (Li and Weisberg 1999; He and Weisberg 2002b). In this framework, the experimental design using WERA is described in section 2 with observations given in section 3. In section 4, radial and vector surface and subsurface currents are compared from the August

TABLE 1. Capabilities of the 16- and 30-MHz WERA systems. Beam forming (BF) using a phased array is needed for wind and wave measurements compared to the direction finding (DF) where the array is arranged in a square.

	16 MHz	30 MHz
Operation range (km from radar site)	80	45
Range cell resolution (km)	1	0.3
Measurement depth (m)	0.7	0.4
Measurement cycle (min)	<10	<10
Radial current (cm s^{-1})	2	2
Vector current (cm s^{-1})	5	5
Vector direction ($^{\circ}$)	± 3	± 3
Bragg wavelength (m)	9.34	5
Transmit elements (Yagi)	4	4
Receive elements (BF)	8–16	8–16
Receive elements (DF)	4	4
Transmitter peak power (W)	30	30

and September 2003 experiment. Tidal and wind effects are addressed in section 5, with a summary of results and concluding remarks in section 6.

2. Measurement approach

An HF-radar experiment was conducted in the summer of 2003 over the WFS using WERA (Gurgel et al. 1999a,b). In this section, the experimental design including WERA and ADCP mooring specifications are described.

a. WERA characteristics

WERA transmits a frequency modulated continuous wave (FMCW) chirp at 0.26-s intervals and avoids the blind range in front of the radar of interrupted FMCW (Gurgel et al. 1999b; Essen et al. 2000). The range of frequencies used for WERA is from 3 to 30 MHz with more common transmission frequencies of 16 and 30 MHz corresponding to Bragg wavelengths of 9.4 and 5 m, respectively (Table 1). At a transmission frequency of 16.045 Hz, the WERA system requires 102-m (139-m) baseline distance for a 12- (16-) element phased array to achieve a narrow beam, electronically steered over the illuminated ocean footprint. Beamwidth is a function of the radar wavelength divided by the length of a phased array, which is 10° and 7.5° for the 12- and 16-element phased arrays, respectively. The transmitter is arranged to encompass a 120° swath. WERA has the flexibility to be configured in DF mode (such as CODAR) where four receiver antennas are set up in a square array, or in BF mode from a linear array consisting of $4n$ (where $n = 2, 3, 4$) elements or channels. As the number of receiver antennas' elements increase, current vector resolution improves (Teague et al. 2001). A medium-range, high-horizontal-resolution version has been designed where the range is ≈ 80 km with

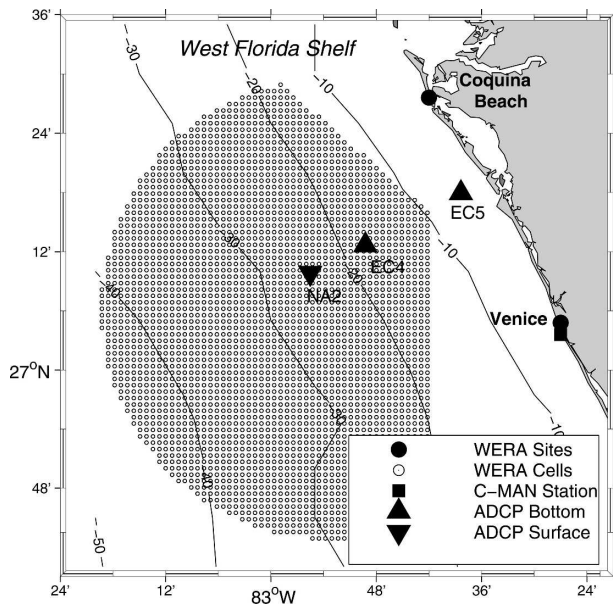


FIG. 1. WERA domain (open circles) for vector currents relative to USF ADCP bottom moorings (EC4, EC5: triangles), NA2 surface mooring (inverted triangle), and C-MAN station (square). WERA master (slave) sites (darkened circles) at the Venice Sewage Treatment Facility (Coquina Beach) during August and September 2003.

horizontal resolution of 1.2 km depending on the available bandwidth approved by the Federal Communications Commission. Higher spatial resolution requires bandwidth of more than 200 kHz (i.e., ± 100 kHz). Temporal sampling can be as low as a few minutes as the WERA system is FMCW. This sampling feature is attractive for high-current regimes such as the Florida Current where time scales of variability are less than an hour associated with large horizontal shear vorticities (Peters et al. 2002).

b. WFS experimental design

A dual-station WERA system was deployed along the WFS starting 23 August and ending 25 September 2003 to sense the surface circulation over moored ADCPs. During this period, a 33-day nearly continuous time series of radial and vector surface currents were acquired at 30-min intervals. At a transmit frequency of 16.045 MHz, the HF radar system mapped coastal ocean currents over a $40 \text{ km} \times 80 \text{ km}$ domain at 2820 cells (Fig. 1). Radar sites were located in Venice, Florida, adjacent to the City of Venice Sewage Treatment Facility ($27^{\circ}4.71'N$, $82^{\circ}27.05'W$) and at an ocean-front site along Coquina Beach, Florida ($27^{\circ}27.36'N$, $82^{\circ}41.7'W$), equating to a baseline distance of 45 km (i.e., \approx half the radar range). Each site consisted of a 4-element transmit and a 16-element receiving array (spaced 9.34 m apart) oriented at angles of 251° (from

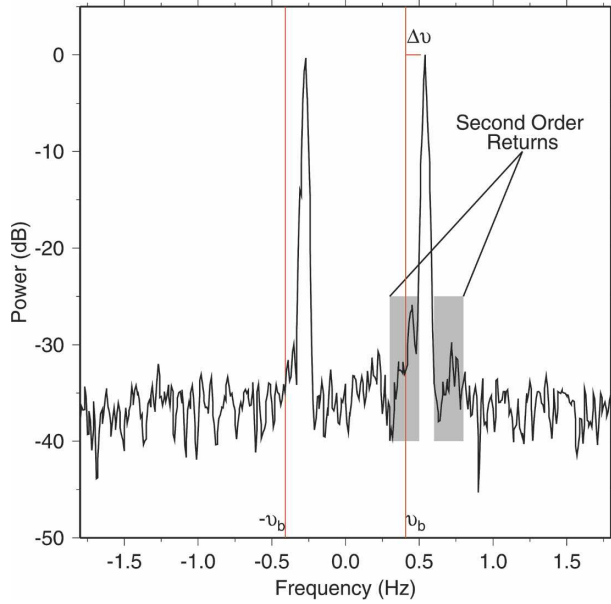


FIG. 2. Doppler spectrum from the WERA WFS deployment from a cell located 40 km offshore showing the spectral peaks in power (dB) relative to the frequency (Hz). Bragg frequencies are depicted as $\pm\nu_b$ at 0.408 Hz as well as the frequency offset ($\Delta\nu$). Frequency offsets of the spectral peaks for the advancing and receding wave field correspond to the radial current. Second-order returns contain information about the waves.

true north (T) at Venice and 240°T at Coquina Beach. Cable calibrations were conducted at the beginning, during, and at the end of the deployment to monitor any variations in signal amplitudes and phases.

c. Radial and vector currents

The Bragg frequency is given by

$$\nu_b = \sqrt{\left(\frac{g\nu_r}{\pi c_o}\right)}, \quad (1)$$

where g is the acceleration of gravity (9.81 m s^{-2}), and ν_r is the radar frequency (16.045 MHz). The resultant Bragg frequency is 0.408 Hz (Fig. 2). Frequency offsets from this first-order, Bragg peak ($\Delta\nu = \nu_o - \nu_b$) are proportional to the radial current for a wave advancing (positive) or receding (negative) from the radar station (i.e., $\Delta\nu = 2V_{cr}\lambda^{-1}$, where V_{cr} is the radial component of current along the direction of the radar). Given the range in the Doppler spectrum of ± 1.75 Hz, the maximum resolvable radial current is $\pm 16.3 \text{ m s}^{-1}$. The first-order returns were above the Doppler spectra noise floor (≈ -40 dB) for both advancing and receding waves. At least two radar stations are required to provide the radial current from the Doppler spectra to calculate the two-dimensional vector current.

Central to constructing reliable vector current fields from radial measurements is the intersection angle between the radials emanating from each radar station (Fig. 3). These intersection angles depend on beach topography, which sets the phased array's geometrical constraints. In this HF radar domain, acceptable intersection angles, defined here as $30^\circ \leq \alpha \leq 150^\circ$, encompassed nearly the entire domain except for grid points closest to the shore, and those just beyond the 40° limits in the northwest and southwest corners of the HF radar domain. These outer limits were at the maximum range of the radar stations of ≈ 80 km (Table 1). The Geometric Dilution of Precision (GDOP) is used to quantitatively examine the spatial difference between an HF-radar-derived current and an ideal point measurement of current from a mooring or ship based on geometrical constraints. Using the radar's mean look direction (α), and the half-angle (ϕ) between intersecting beams, Chapman et al. (1997), derived expressions for the error in the u and v current components:

$$\sigma_u = \left[2 \frac{\cos^2(\alpha)\sin^2(\phi) + \sin^2(\alpha)\cos^2(\phi)}{\sin^2(2\phi)} \right]^{(1/2)} \sigma, \quad (2)$$

and

$$\sigma_v = \left[2 \frac{\sin^2(\alpha)\sin^2(\phi) + \cos^2(\alpha)\cos^2(\phi)}{\sin^2(2\phi)} \right]^{(1/2)} \sigma, \quad (3)$$

where σ represents RMS current differences. The GDOP value is defined as the ratios of (σ_u/σ) and (σ_v/σ) for the u and v current components, respectively. Over the HF-radar domain (Fig. 3b), the GDOP ranged from 1 to 2.25. In the core of the domain where ADCP measurements were acquired, the GDOP for both the current components ranged from 1 to 1.25. Close to the coast, however, there was a large GDOP gradient of 1 to 2 over a few kilometers distance as intersection angles approached 150° (Fig. 3a).

As each cell ($1.2 \text{ km} \times 1.2 \text{ km}$) has its own unique bearing and distance from each site (i.e., Fig. 3a), the east–west current at any given cell is

$$u = \frac{r_v \cos(\theta_c) - r_c \cos(\theta_v)}{\sin(\theta_c - \theta_v)}, \quad (4)$$

and the north–south current is

$$v = \frac{r_c \sin(\theta_v) - r_v \sin(\theta_c)}{\sin(\theta_c - \theta_v)}, \quad (5)$$

where $r_{v,c}$ represent radial currents and $\theta_{v,c}$ represent bearing angles relative to the bore sites from the Venice

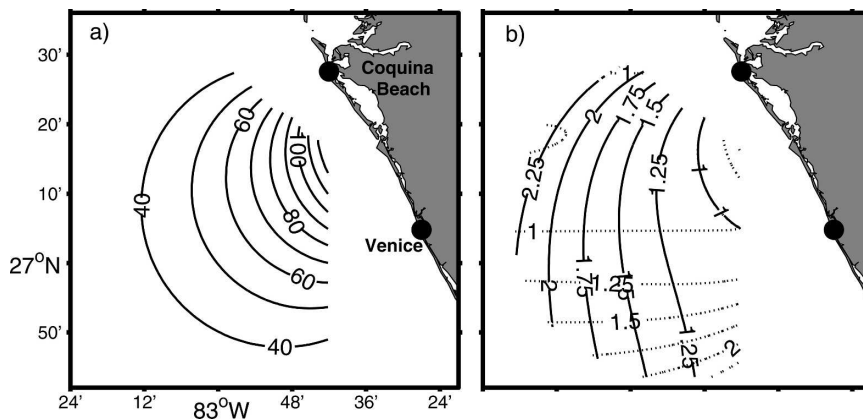


FIG. 3. (a) Intersection angles ($^{\circ}$) and (b) GDOP for the u component (solid) and v component (dashed) at the WERA cells. The contour interval for the intersection angle is 10° intervals, and the nondimensional GDOP is 0.25 increments.

and Coquina Beach stations, respectively. As shown in Fig. 4, the returns of the vector current field ($w = u + v$) are constructed from (4)–(5) based on observed radial currents and bearing angles (Fig. 3a). Vector current retrievals exceeded 70% over the entire footprint, and more importantly exceeded 90% in the central part of the WERA domain over the COMPS moorings (Weisberg et al. 2002). Over the course of the experiment, a total of 1628 half-hourly samples were acquired from 0320 UTC 23 August [yearday (YD) 235] until 2340 UTC 25 September (YD 269). During the experiment, only 70 samples were missing from the vector time series, equating to a 4.2% loss of the snapshots. Previous experiments have typically yielded data returns to construct surface current vectors 93%–97% of the time (Haus et al. 2000; Shay et al. 2002; Martinez-Pedraja et al. 2004).

d. Radial current accuracy

For n samples of a radial current [$r(i)$] consisting of N_f spectral lines in the Doppler spectrum with a signal-to-noise ratio [SNR(i)], radial current accuracy can be estimated. In the beam-forming mode, n samples are from $\pm (N_f/64)$ so $n = (N_f/16) + 2$. From these n samples, the average r is

$$\bar{r} = \frac{\sum_{i=1}^n r(i) \text{SNR}(i)}{\sum_{i=1}^n \text{SNR}(i)}, \quad (6)$$

and its variance is

$$r_{\sigma} = \sqrt{\frac{\sum_{i=1}^n r^2(i) \text{SNR}(i)}{\sum_{i=1}^n \text{SNR}(i)} - \bar{r}^2}. \quad (7)$$

The accuracy is given by $r_{\sigma} \sqrt{n^{-1}}$ for each of the radar site (K.-W. Gurgel 2006, personal communication). For each sample interval in time, radial current accuracy is estimated by accounting for signal strength as well as horizontal shear within a grid cell. This approach also uses the variance of the current velocity (i.e., the change over the integration time) in estimating accu-

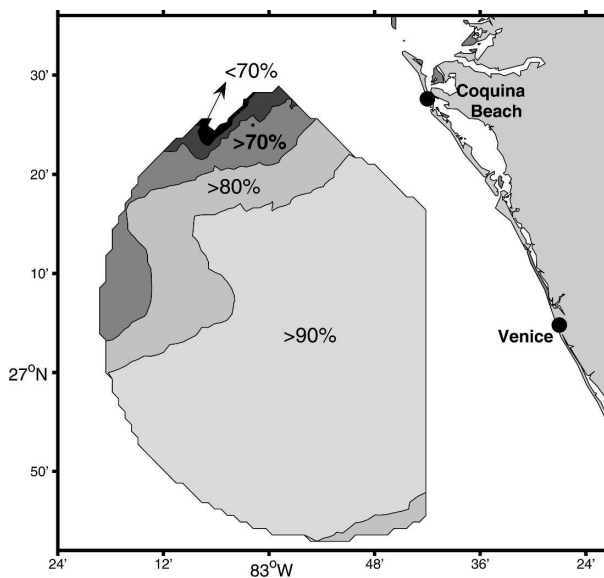


FIG. 4. Percent of time the vector current maps were acquired by WERA during the WFS experiment in August and September 2003.

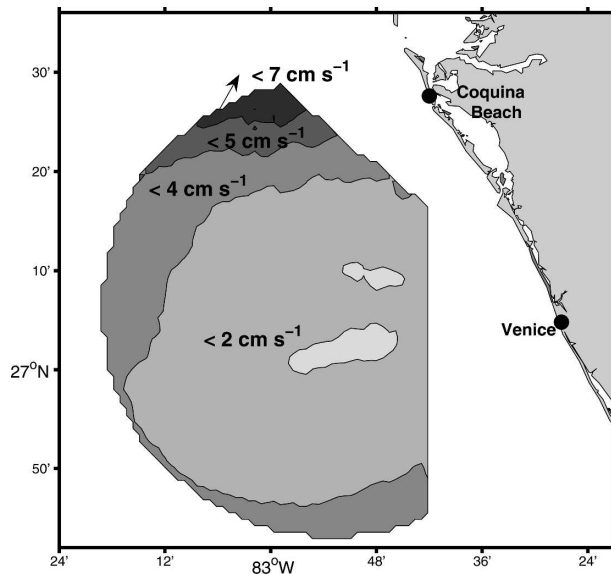


FIG. 5. Radial current accuracy (cm s^{-1}) from WERA averaged from 33 days of measurements from the master (Venice) and the slave (Coquina Beach) based on signal strength.

racy of the radial current measurement. The magnitude of the radial current accuracy is combined through the sum of the squares from each snapshot ($r_{sc}^2 + r_{sv}^2$) then time averaged over the domain (Fig. 5). Time average of accuracy reduces the influence of horizontal shear, and over the core of the radar domain, radial current accuracy ranged from 2 to 3 cm s^{-1} , suggestive of high-quality surface current measurements. As the far field is approached from Venice (northern part of the domain), radial current accuracy decreases to 5 to 7 cm s^{-1} . Generally, higher data accuracy is acquired close to the coast and over the mooring sites as signal strength attenuates seaward away from the radar sites (Broche et al. 1987; Gurgel et al. 1999a,b).

e. Moored measurements

As part of the COMPS program, moored ADCP arrays are maintained to understand the long-term circulation patterns over the WFS shown in Fig. 1 (Weisberg et al. 2002). One set of current profiles is from an upward-looking ADCP mounted on a fixed bottom rack at the 20-m isobath (EC4), and the other instrument package is from a downward-looking ADCP mounted on a surface mooring at the 25-m isobath (NA2). Both emplacements used similar instruments: RD-Instruments, 300-kHz Workhorse ADCPs, sampling at 1 Hz for 300 pings per hourly ensemble from which one-hourly velocity vector profile determination is made. Comparison tests between similar upward- and downward-looking deployments on the same WFS iso-

bath demonstrate less than 2 cm s^{-1} differences (within the manufacturers specifications) for these two deployment methods. For both deployments, the velocity profile data, sampled at 0.5-m intervals, were edited for near-surface and near-bottom reflection effects, and then linearly interpolated to 1-m bins. Near-surface velocity measurements are compromised by sidelobe reflection, and for the case of the downward-looking ADCP, the near-surface layer is missed by a combination of buoy geometry and an acoustic noise-related blanking distance (transit time) from the transducers to the first bin sampled. Horizontal velocity vectors from the 20- and 25-m isobath sites were available between 4 and 17 m and between 4 and 22 m of the surface, respectively. Record lengths at these two moorings are of several years duration (see <http://ocg6.marine.usf.edu>), and the deployment coinciding with this WERA test was subsampled to provide the comparison data used here. In addition to the oceanic measurements, the NA2 mooring also housed an Air–Sea Interaction Meteorological (ASIMET) sensor suit, designed by the Woods Hole Oceanographic Institution. Of particular interest here are the wind speed and direction measurements using an RM Young 5103 wind module located at 2.8 m above the surface.

3. Observations

Observations include surface currents from WERA, surface winds from three sites, and subsurface currents from ADCP moorings. To facilitate comparisons between surface and subsurface currents, half-hourly surface current measurements are smoothed by a three-

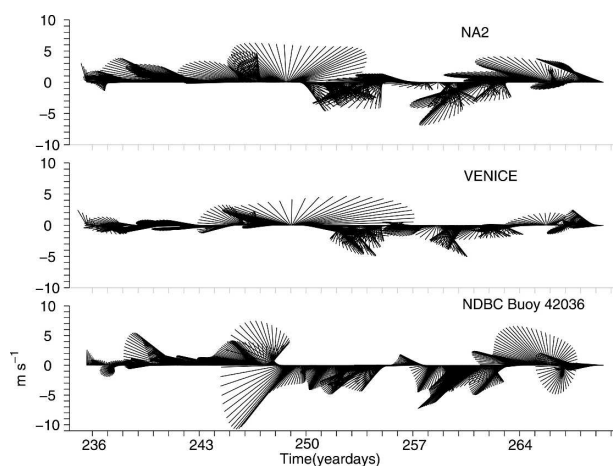


FIG. 6. Twenty-four-hour low-pass-filtered 10-m surface wind (m s^{-1}) at NA2, Venice Pier, and an NDBC buoy rotated into an oceanographic context (positive is north) during the August and September 2003 experiment over the WFS.

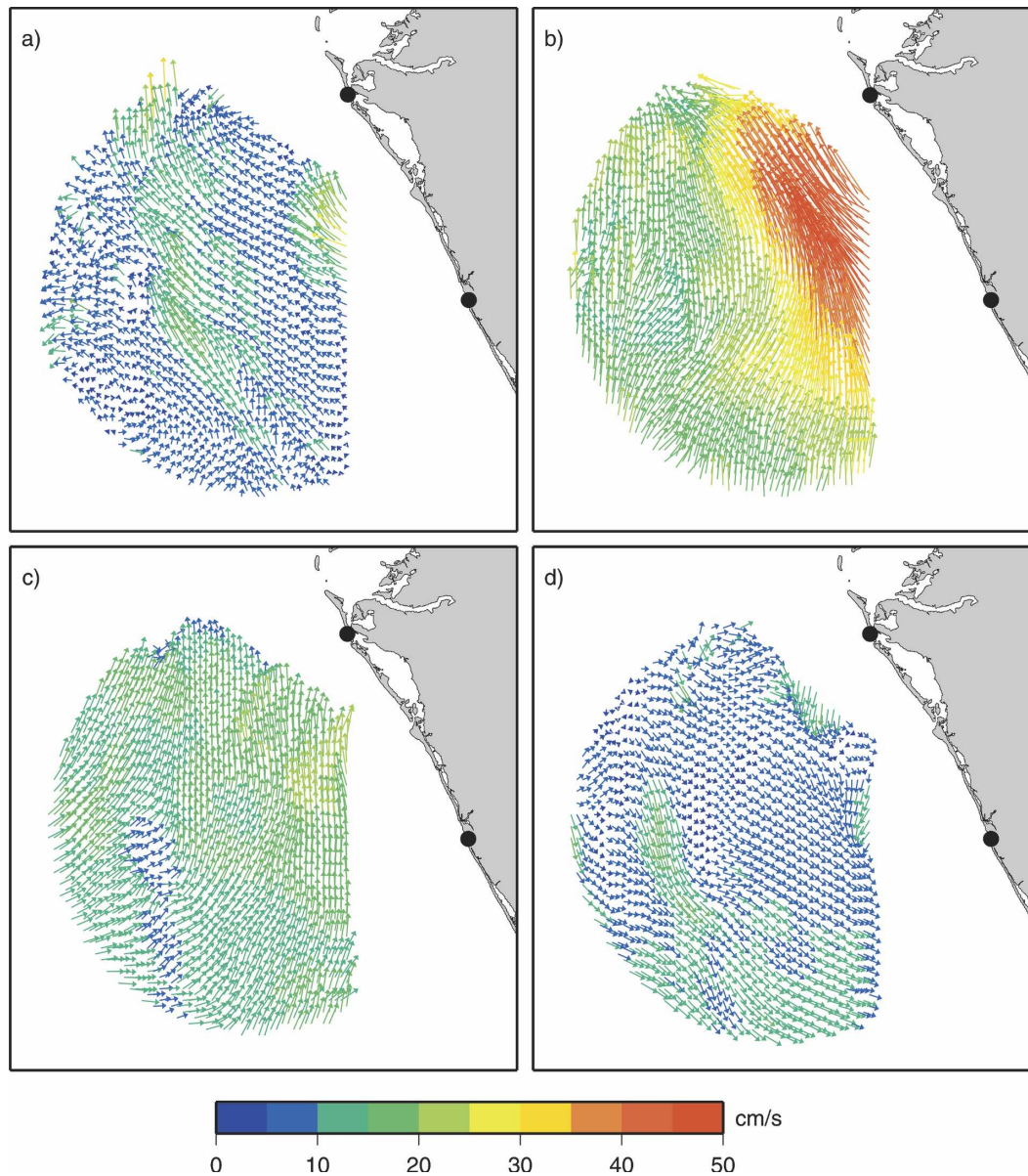


FIG. 7. Evolution of surface currents for (a) 1700 UTC 29 Aug, (b) 1800 UTC 5 Sep, (c) 0400 UTC 6 Sep, and (d) 0200 UTC 8 Sep 2003. Note that Tropical Storm Henri passed northwest of the radar domain on 5 Sep and made landfall north of Tampa Bay. Color bar depicts current magnitude in cm s^{-1} .

point Hanning window and subsampled at hourly intervals to coincide with ADCP-measured current structure.

a. Surface wind and stress

Prevailing atmospheric conditions during the experiment were relatively calm as indicated by 24-h low-pass-filtered wind records adjusted to 10 m from the Venice Pier, the NA2 surface mooring (more details below), and National Data Buoy Center (NDBC) buoy

42036 (Fig. 6). The NDBC buoy was located at $28^{\circ}30.37'N$, $84^{\circ}30.62'W$, northwest of the radar domain. The NA2 surface buoy was located in the central portion of the radar footprint. Over the 33-day record, a mean wind of 4.7 m s^{-1} was directed toward the west-northwest at $\approx 310^{\circ}$. During the passage of Henri, northward surface winds exceeded 8 m s^{-1} at NA2 and approached 12 m s^{-1} at the NDBC buoy (farther offshore)—both sites were well away from the low pressure center. The averaged wind stress components,

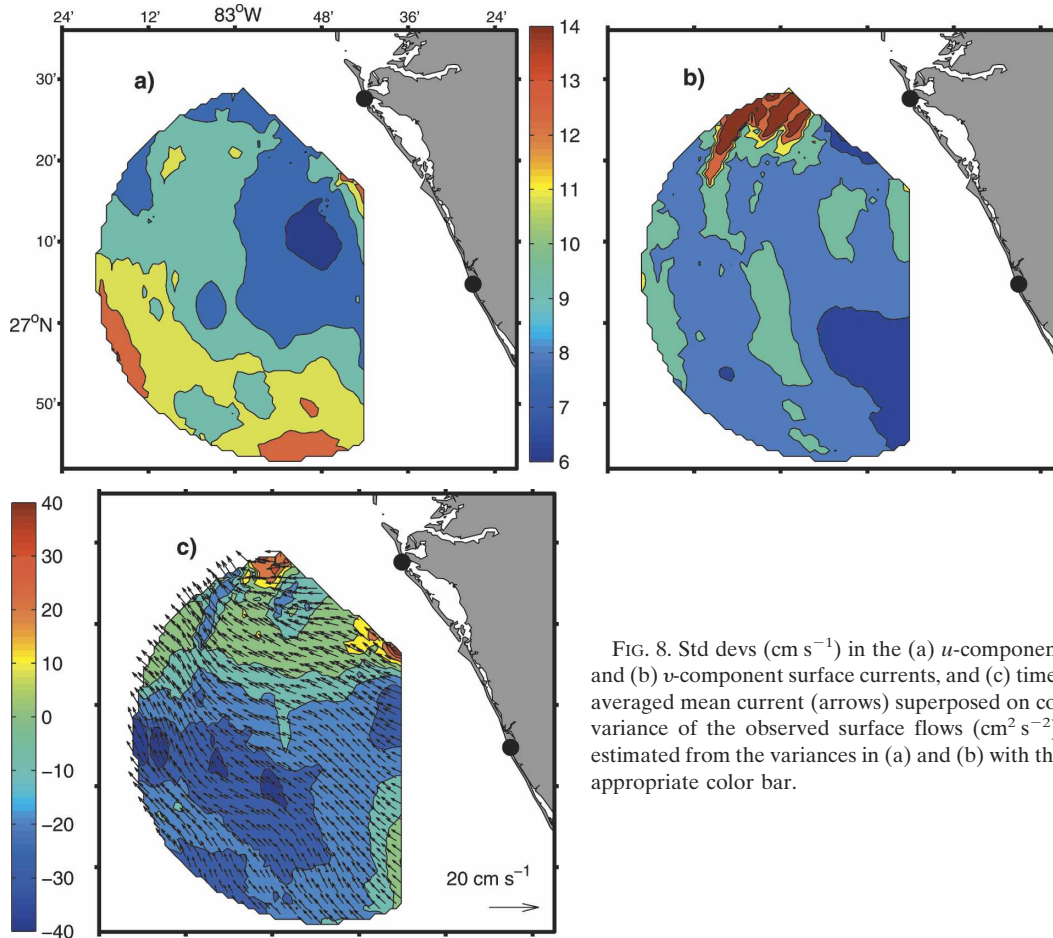


FIG. 8. Std devs (cm s^{-1}) in the (a) u -component and (b) v -component surface currents, and (c) time-averaged mean current (arrows) superposed on covariance of the observed surface flows ($\text{cm}^2 \text{s}^{-2}$), estimated from the variances in (a) and (b) with the appropriate color bar.

based on the Fairall et al. (1996) algorithm, were -2.6×10^{-2} and $2.4 \times 10^{-3} \text{ N m}^{-2}$ in the east–west and north–south directions, respectively. This mean wind stress direction toward the west–northwest is consistent with surface winds derived from a summer climatology (Yang and Weisberg 1999).

b. Surface currents

An example of the observed surface current variability is shown in Fig. 7 over a 10-day period, including the passage of Tropical Storm Henri on 5 September. On 29 August (YD 240), surface velocities ranged between 15 and 25 cm s^{-1} over the radar footprint with flows directed toward the northwest. As Henri approached, cyclonically rotating winds forced northward surface flows with maximum surface currents over the inner shelf of more than 40 cm s^{-1} on 5 September (YD 247). Over the outer part of the domain, surface currents were directed shoreward after 2 h. On 6 September (YD 248), surface velocities of 25 cm s^{-1} were observed to have an east to northeast orientation as the winds

relaxed (Fig. 7c). By 8 September (YD 250), surface currents decreased to pre-Henri levels of 15 to 20 cm s^{-1} . Of particular interest are the along-shelf structure and the patchiness in the surface currents that may be due to transient surface winds that occur over the WFS during the summer months. These surface velocity images exemplified an energetic and coherent coastal ocean response to surface winds.

To further illustrate this spatial surface current variability, the standard deviation and covariance of the surface velocity field are estimated from the entire time series (Fig. 8). The standard deviations of the u (Fig. 8a) and v (Fig. 8b) components differed by a factor of 2 depending on their location in the radar domain. The standard deviation in the u component was a maximum of 10 cm s^{-1} in the far field. Over the central and inner portions of the footprint, standard deviations decreased to between 6 to 8 cm s^{-1} . In the v component, the standard deviation was similar except in the north-central portion of the domain where the standard deviations exceeded 15 cm s^{-1} . Note that this region is located in

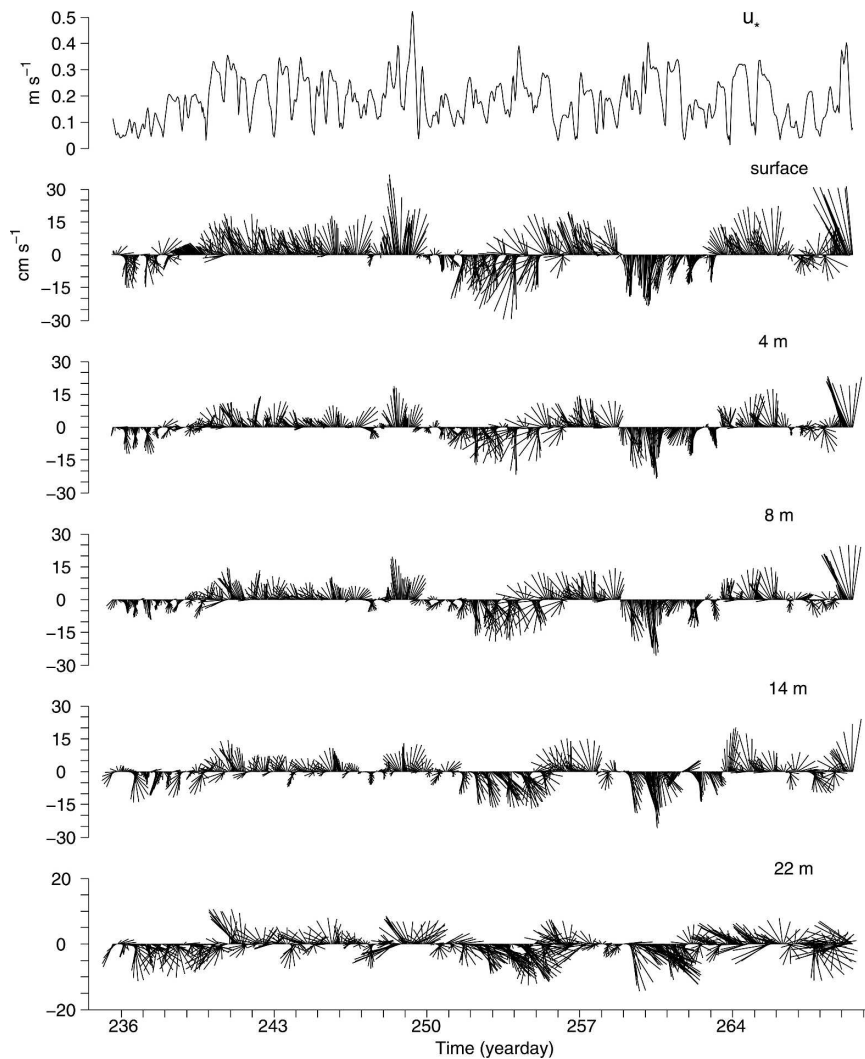


FIG. 9. Surface friction velocity (u_* ; m s^{-1}) and vector current (cm s^{-1}) time series located at the NA2 ADCP mooring position for the surface (WERA cell 1816), 4, 8, 14, and 22 m during the WFS experiment in August and September 2003.

the far field of the Venice site, and caution needs to be placed on these current estimates. However, this region is also closest to Tampa Bay and may be influenced more by the semidiurnal and diurnal tidal currents. While time-averaged mean currents were slightly stronger in the northern part of the domain, mean flows indicated a general northwest mean current of 10 to 15 cm s^{-1} , which is displaced to the right side of the mean wind stress direction of west-northwest described above in accord with wind-driven flows. The covariance ($u'v'$) was negative over about 60% of the domain. However, covariances ranged from 10 to 20 $\text{cm}^2 \text{s}^{-2}$ in the northern part of the radar domain. These results are consistent with the WFS summertime circulation as described by Yang and Weisberg (1999) and more recently by Liu et al. (2007).

c. Vertical ocean structure

As shown in Fig. 9, coherent current structure was observed to 22-m depth at the NA2 mooring. Surface currents ranged from -30 to 35 cm s^{-1} where larger currents were observed during Henri's passage. At 4-m depth, the current ranged from $\pm 15 \text{ cm s}^{-1}$, decreasing to $\pm 10 \text{ cm s}^{-1}$ at 22-m depth. In the upper 8 m, there is evidence of a Henri response on YD 247 when the surface friction velocity (u_*) exceeded 0.5 m s^{-1} based on Fairall et al. (1996). Subsequent to Henri, weak current oscillations were detected at the mooring excited during storm passage that may be associated with the near-inertial response (inertial period $\approx 26 \text{ h}$). Surface friction velocities over the remainder of the time series ranged between 0.1 to 0.3 m s^{-1} corresponding to wind

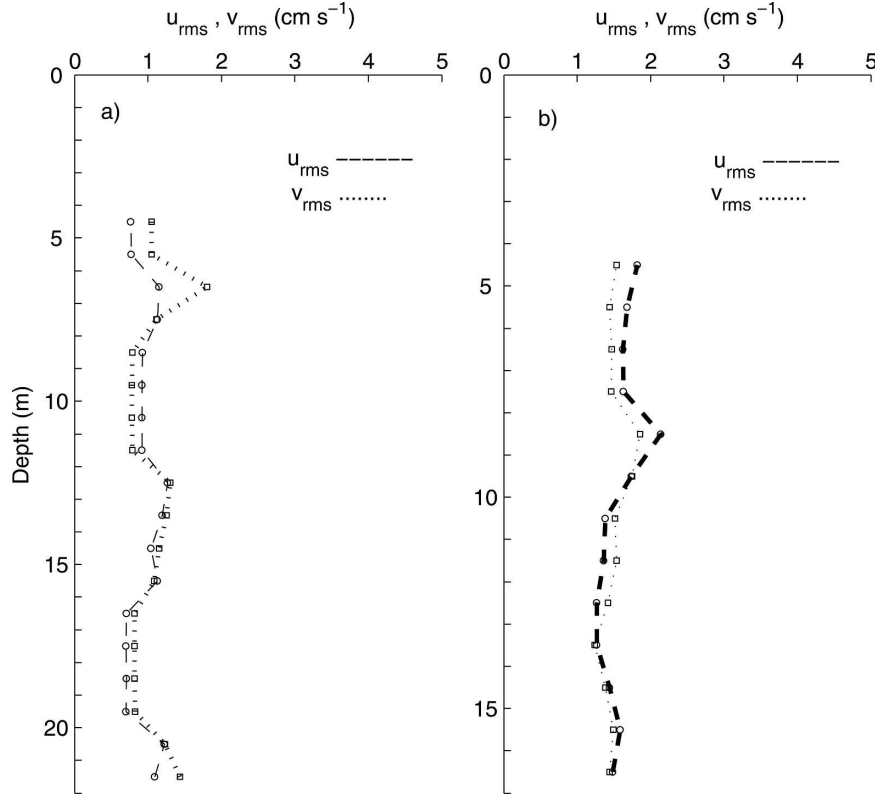


FIG. 10. Profiles of bin-to-bin RMS current differences (cm s^{-1}) from (a) NA2 and (b) EC4 ADCP moorings for the u (dashed) and v (dotted) components.

stresses between -0.1 and 0.16 N m^{-2} . At both moorings, bin-to-bin RMS differences were typically 1 to 2 cm s^{-1} over the depth ranges of 17 and 22 m (Fig. 10). For example, differences were $\approx 1 \text{ cm s}^{-1}$ except between 6 and 7 m when the differences increased to about 2 cm s^{-1} in the v component at NA2. At EC4, the RMS differences were slightly higher ranging between 1.5 to 2 cm s^{-1} in the upper 9 m . These results suggest that the ADCP current measurements were representative of current structure variations over the WFS.

4. Comparisons

Observations indicated sufficient veracity to warrant a detailed comparison between radar-derived surface signals over a 1.44-km^2 area and subsurface measurements from two cross-shelf ADCP moorings. One statistical measure of the correlation between two differing vector measurements is the complex correlation coefficient:

$$\gamma = \frac{\langle u_s u_b + v_s v_b \rangle + i \langle u_s v_b - v_s u_b \rangle}{\langle u_s^2 + v_s^2 \rangle^{(1/2)} \langle u_b^2 + v_b^2 \rangle^{(1/2)}}, \quad (8)$$

and the complex phase angle,

$$\phi = \tan^{-1} \frac{\langle u_s v_b - v_s u_b \rangle}{\langle u_s u_b + v_s v_b \rangle}, \quad (9)$$

where $\langle \dots \rangle$ represents an average (based upon n points) (Kundu 1976) for the WERA surface (s) currents to 0.7 m and subsurface (b) ADCP-derived currents at 4 m at both NA2 and EC4 moorings. This phase angle represents the average cyclonic angle of the subsurface current vector with respect to the surface current vector. Standard R^2 values are estimated for radial current comparisons.

a. Radial series

Radial currents from each radar site are compared to radial currents determined from the ADCP measurements at 4 m (Fig. 11). (Kinetic energy conserved in coordinate rotation.) Comparisons at EC4 indicate good agreement using radial currents from Coquina Beach ($\theta = 204.5^\circ$) and Venice Beach ($\theta = 292^\circ$). In general, radial currents from the Coquina Beach site indicate slightly better comparisons as the surface and 4-m currents track between -30 (during Henri) and 20 cm s^{-1} . The RMS difference (Table 2) was 3.4 cm s^{-1} based on 814 data points. Relative to the Venice site,

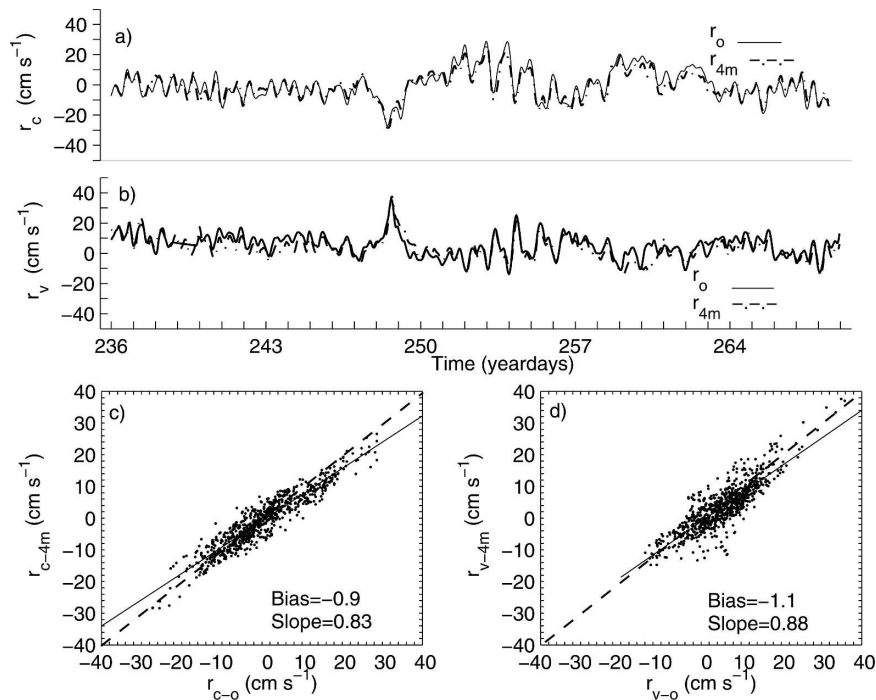


FIG. 11. Comparison of radial surface (r_o ; solid) and 4-m currents (r_{4m} ; dashed-dotted) for time series for EC4 from (a) Coquina Beach ($\theta = 204.5^\circ$) and (b) Venice ($\theta = 292^\circ$) and their regression analyses for (c) Coquina Beach and (d) Venice between surface (r_o) and 4-m depth (r_{4m}) in cm s^{-1} where dashed (solid) curve represents ideal (actual) slopes.

radial currents ranged between -10 and 40 cm s^{-1} with the larger values occurring during Henri. Both surface and 4-m radial currents track well over the time series with an RMS difference of 4.4 cm s^{-1} . Similar results were obtained for the NA2 mooring with RMS differences between 4.1 and 5.4 cm s^{-1} for Coquina Beach ($\theta = 214.7^\circ$) and Venice ($\theta = 281.5^\circ$), respectively. The R^2 were 0.92 and 0.81 for these radial current comparisons.

Regression analyses between the surface and 4-m radial currents (Figs. 11c,d) indicate a bias of -0.9 cm s^{-1} and a slope of 0.83 relative to Coquina Beach. Radial currents from the Venice site indicate similar results with a bias of -1.1 cm s^{-1} with a slope of 0.88 . Both sets

TABLE 2. Comparison of radial currents between the surface current (r_o) and subsurface current (r_{4m}) at EC4 and NA2 relative to bearing angles from Venice and Coquina Beach for mean differences, RMS differences, and the correlation coefficient (R^2) based on the 33-day time series ($N = 814$ points).

Series	Bearing ($^\circ$)	$r_o - r_{4m}$ (cm s^{-1})	$(r_o - r_{4m})_{\text{RMS}}$ (cm s^{-1})	R^2
NA2-C	214.7	0.01	4.1	0.92
NA2-V	281.5	2.8	5.4	0.81
EC4-C	204.5	0.9	3.4	0.94
EC4-V	292.0	1.7	4.4	0.86

of radial currents at EC4 reveal little scatter with similar results observed at the NA2 mooring. Notice that the perfect comparison (bias = 0, slope = 1) suggests a slight offset between surface and 4-m currents. Thus, surface and 4-m radial current comparisons indicate sufficient veracity for the two-dimensional vector current comparisons at the two ADCP sites.

b. Vector series

As shown in Fig. 12, surface current components are compared to 4-m subsurface currents at the NA2 mooring. The u components ranged between 10 and -25 cm s^{-1} , and were weaker than the v component. The maximum northward surface current observed during Tropical Storm Henri on YD 247–248 approached 40 cm s^{-1} compared to 20 cm s^{-1} at 4 m. The southward current was a maximum of about 25 cm s^{-1} , suggestive of background variability in the north–south direction than in the east–west direction. During Henri's closest approach, this resulted in a bulk current shear of $5 \times 10^{-2} \text{ s}^{-1}$ (Fig. 12c). These levels of bulk current shear between surface and near-surface current measurements have been documented in other coastal regimes influenced by the Gulf Stream and Florida Current (Shay et al. 1995, 2002) as more dense, subtropical wa-

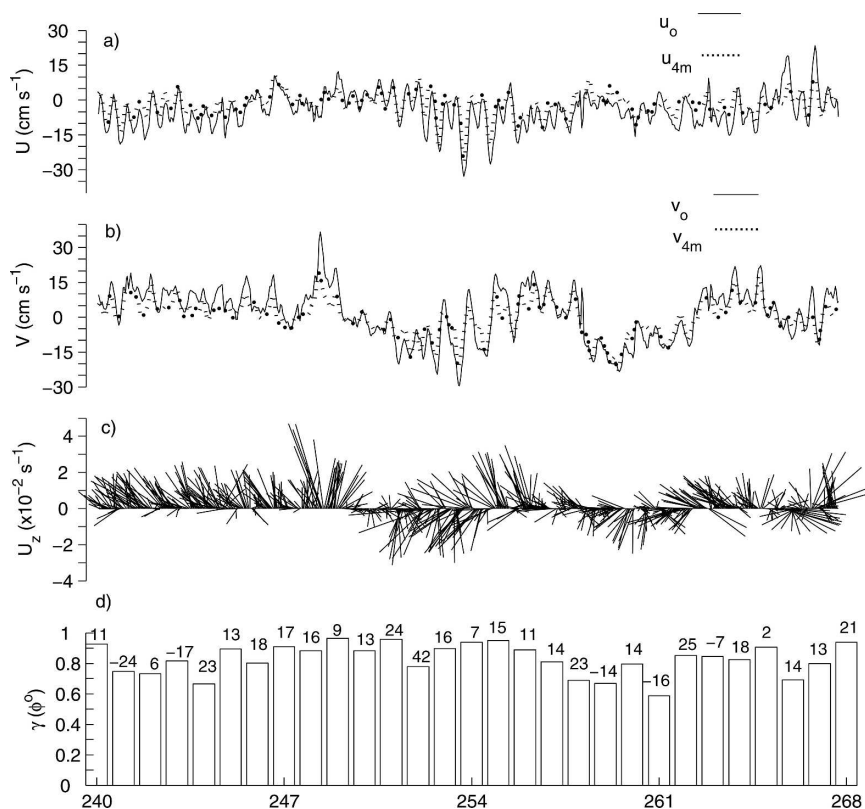


FIG. 12. Comparison of WERA-derived surface ($_{s}$; solid) and 4-m subsurface ($_{4m}$; dotted) current time series from the surface ADCP mooring at NA2 for the (a) u component (cm s^{-1}), (b) v component (cm s^{-1}), (c) bulk current vector shear ($\times 10^{-2} \text{ s}^{-1}$) defined as current differences within (a) and (b) divided by a depth difference of 3.25 m, and (d) daily complex correlation coefficients (γ) and phase angles [$\phi(^{\circ})$: located at the top of the bars] relative to the surface velocity. A negative phase implies an anticyclonic current veering with depth.

ter is subducted underneath the fresher, coastal waters (Marmorino et al. 1998). Subsequent to Henri, the currents oscillated with a frequency close to the local inertial period (26.4 h) in both the surface and subsurface layers. Over the 33-day series, surface and subsurface currents were well correlated with values exceeding 0.80 from (8). However, on YD 261, the correlation coefficient decreased to below 0.7, which may be in part due to a weaker u component of current. Complex phases ranged from -17° (anticyclonic veering with depth) to 42° (cyclonic veering with depth) as per (9). Similar trends in the data were observed at the 4-m level at the EC4 mooring.

Current data from 4-m depth were regressed to the surface current measurements (Fig. 13). At EC4, the scatter for the u component revealed a slope of 0.8 with a bias of -2 cm s^{-1} . Similarly, the slope was $O(1)$ in the v component (Fig. 13b) where the bias was -0.1 cm s^{-1} . For 814 hourly values, the histogram of the differences reflects this average bias in the distributions. At NA2, the trends are similar in the regression, but with slightly

higher slopes. That is, surface currents tended to be 20% higher than the 4-m-depth currents. Biases ranged from -2.5 to 1.6 cm s^{-1} in the u and v components, respectively. The distributions of the current differences are also similar to those at NA2, suggesting that measurements in the upper few meters of the column were consistent with surface currents averaged over the 1.4-km^2 area.

Surface velocities at the 25-m mooring (i.e., cell 1816 depicted as a triangle in Fig. 1) were used to estimate the complex correlation and phase coefficients as per Eqs. (8)–(9) averaged over the time series at each of the radar cells. As shown in Fig. 14, correlation coefficients followed the orientation of the isobaths with a maximum of 1 at the mooring location. Correlation coefficients decreased from more than 0.7 to about 0.5 in the northern part of the domain. This observed decrease in their respective values is presumably due to weaker far-field returns at the Venice site. By contrast, offshore correlation coefficients remained above 0.6 across the shelf. Phases indicated an anticyclonic current veering

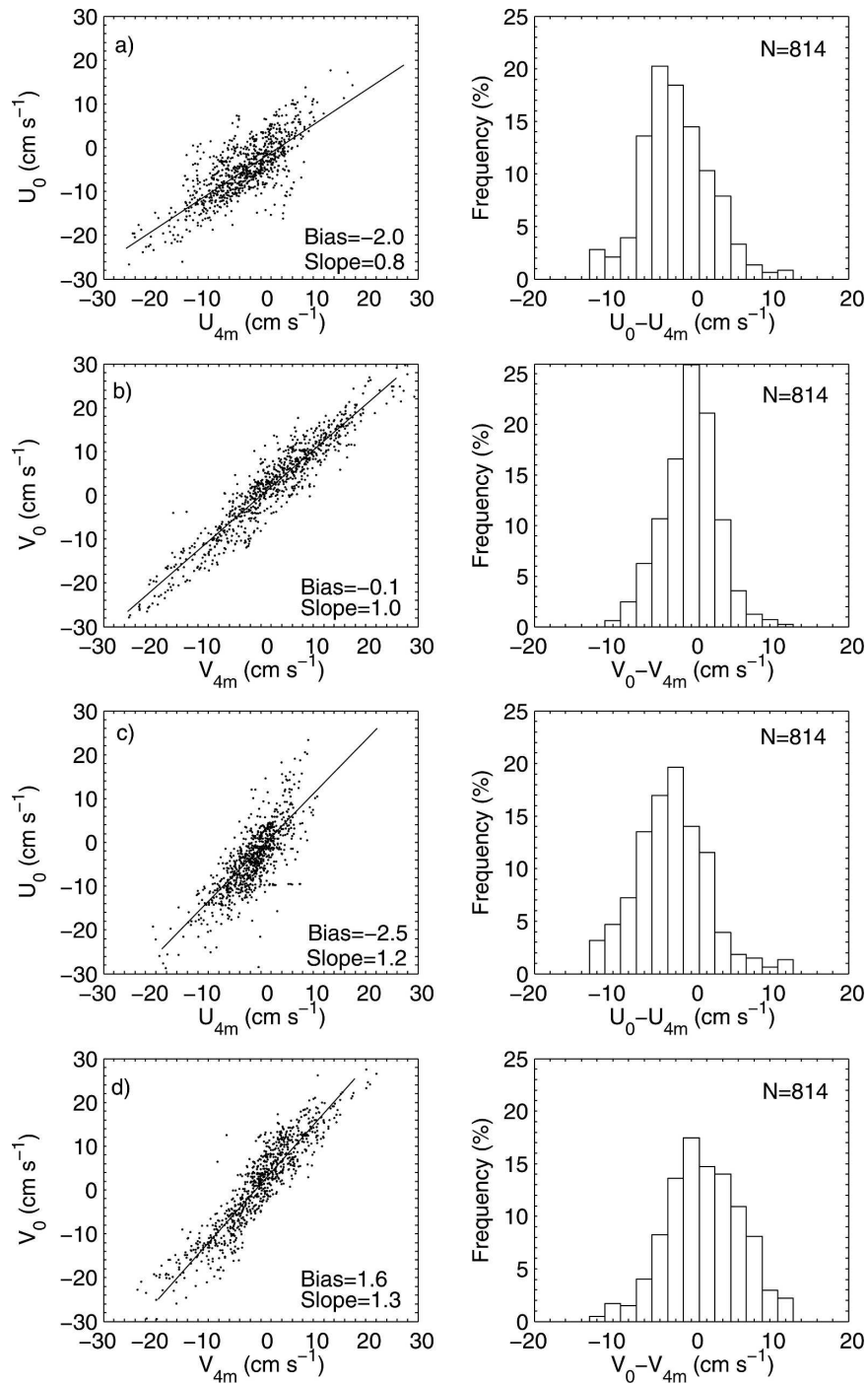


FIG. 13. (left) Scatter diagrams and (right) histograms for the comparisons at EC4 (NA2) for (a), (c) u -component and (b), (d) v -component surface ($_{\circ}$) and subsurface currents ($_{4m}$) along the 20-m (25-m) isobaths, respectively, based on 814 hourly data points in August and September 2003.

relative to 25-m isobath south of NA2 and a cyclonic veering north of the mooring site. The range of the phases was -10° to 10° over most of the domain. Such behavior contrasts with data acquired along the east

Florida shelf where the correlation indices are governed by the time-dependent FC and coherent subscale ocean structures (Shay et al. 2002).

As listed in Table 3, there was a $4.8 (1.7) \text{ cm s}^{-1}$

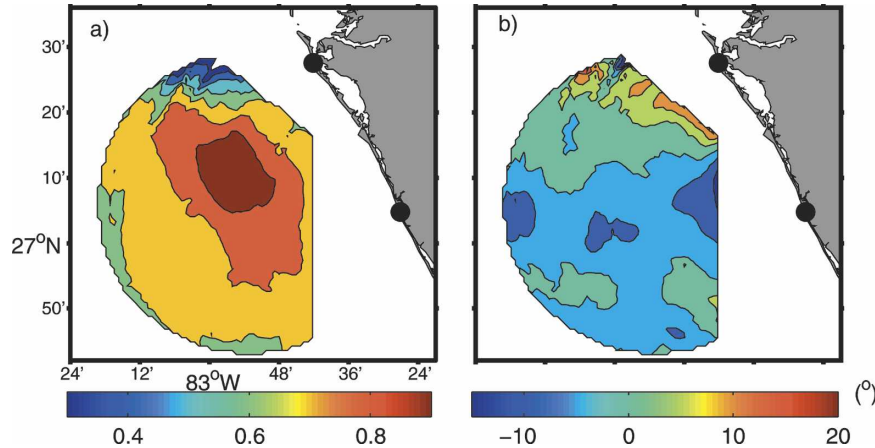


FIG. 14. (a) Complex correlation and (b) phase ($^{\circ}$) relative to the NA2 mooring cell (1816) (inverted triangle; Fig. 1) corresponding to the 25-m mooring for the 33-day time series. Values are given on the color bars, and note that a positive (negative) phase implies cyclonic (anticyclonic) veering relative to cell 1816.

difference between the surface and 4-m current speed at NA2 (EC4). Directional differences were 8° to 10° in the currents, and within the cited accuracy of the system. The u component ranged from -1.9 to -2.5 cm s^{-1} at the two moorings compared to 1.6 to -0.1 cm s^{-1} for the u component. Complex correlation coefficients were ≈ 0.9 with relatively small phases between 5° and -3° at the moorings. Of particular importance, RMS differences were 0.2 to 1 cm s^{-1} in the east-west components, compared to 4.2 to 5.2 cm s^{-1} in the north-south components. Note that the lower values in the u component are due to the lower dynamic range of 10 cm s^{-1} compared to 30 cm s^{-1} in the v component. Comparisons between the surface and near-bottom currents revealed larger differences, but were still considerably less than those reported by Essen et al. (2000). At NA2, the mean current and direction difference was 6 cm s^{-1} and 2° at 22-m depth. While the mean current difference was 4.5 cm s^{-1} at EC4, the directional difference was 18° . A better indicator of this vertical decorrelation was the correlation indices decreased to

0.5 with depth. Based on the RMS differences, this was due to the v component that included accelerated surface currents by Henri and the subsequent near-inertial current response. These differences are clearly reflective of geophysical variability forced by tides and surface winds over the WFS.

5. Physical forcing mechanisms

To examine the physical effects of the tides and winds, tidal currents were determined from the 33-day hourly time series from the measurements following Foreman (1981). Surface and subsurface currents are fit to the dominant semidiurnal and diurnal tidal constituents. The effects of the surface wind and stress on the detided time series are examined at the NA2 mooring where accurate wind measurements were acquired from the ASIMET package.

a. Tidal variations

Since tides over the WFS are mixed with contributions from both diurnal and semidiurnal components,

TABLE 3. Averaged difference between the surface and subsurface currents at NA2 (4 m, 22 m) and EC4 (4 m, 17 m) moorings for speed (V_{o-b}), direction (θ_{o-b}), u component (u_{o-b}) v component (v_{o-b}), complex correlation coefficient (γ), phase (ϕ), and the RMS differences in the east-west ($u_{o-b,rms}$) and north-south ($v_{o-b,rms}$) velocity components based on mooring data during the WFS 2003 experiment ($N=814$ points).

Series	V_{o-b} (cm s^{-1})	θ_{o-b} ($^{\circ}$)	u_{o-b} (cm s^{-1})	v_{o-b} (cm s^{-1})	γ	ϕ ($^{\circ}$)	$u_{o-b,rms}$ (cm s^{-1})	$v_{o-b,rms}$ (cm s^{-1})
NA2 mooring								
V_{4m}	4.8	8.8	-2.5	1.6	0.88	5	0.2	4.2
V_{22m}	6.0	2.0	-4.3	3.0	0.5	-49	1.8	7.2
EC4 mooring								
V_{4m}	1.7	10.0	-1.9	-0.1	0.9	-3	1	5.2
V_{17m}	4.5	17.7	-5.7	2.2	0.52	-55	1.8	10.6

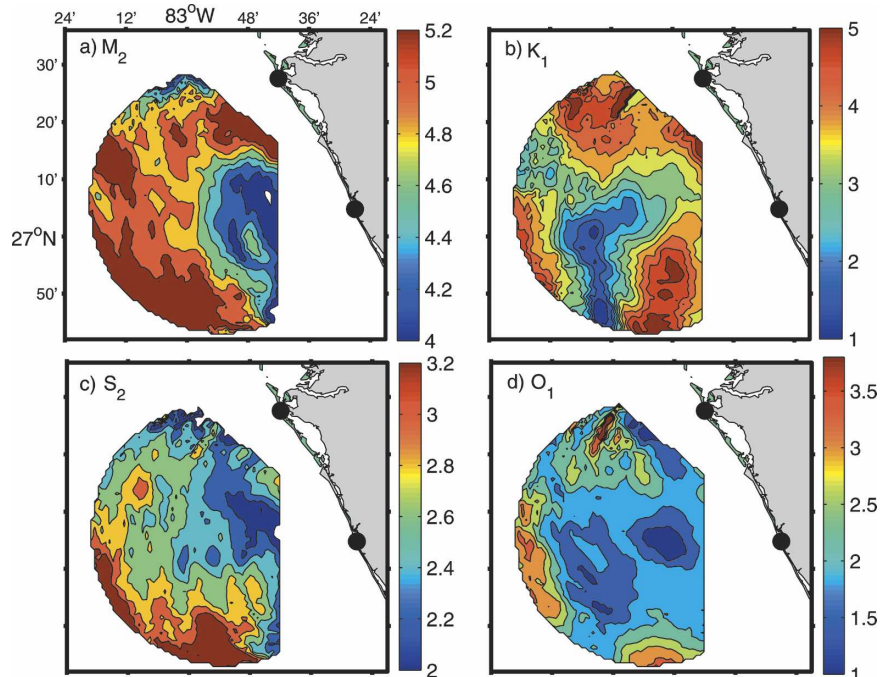


FIG. 15. Amplitudes (cm s^{-1}) of the M_2 , K_1 , S_2 , and O_1 tidal constituents based on a tidal analysis of the surface currents.

the dominant semidiurnal (M_2 , S_2) and diurnal (K_1 , O_1) constituents were analyzed following Foreman (1981). For the M_2 constituent, the current amplitudes ranged from 4 to 5 cm s^{-1} (Fig. 15a). While weaker M_2 tidal amplitudes' contributions were located inshore of the NA2 mooring and south of Tampa Bay, tidal contributions to the currents increased offshore. Except for the relative maxima in the southern part of the domain, the pattern of the S_2 current amplitudes was similar to those of the M_2 , but they were weaker, ranging from 2 to 3 cm s^{-1} . The diurnal tidal currents associated with the stronger K_1 constituent were a maximum of 5 cm s^{-1} in the northern and southern parts of the domain with a minimum of about 1 cm s^{-1} in the south-central portion. The O_1 tidal amplitudes differed considerably, with a minimum oriented in the north-south direction where the O_1 amplitude increased offshore to a maximum of 3.5 cm s^{-1} (Fig. 15d). By constructing the tidal time series of the surface currents based on these constituents, the variance accounted for ranged from a maximum of 40 $\text{cm}^2 \text{s}^{-2}$ to a minimum of 15 $\text{cm}^2 \text{s}^{-2}$ (not shown) over the footprint. Explained variance, defined here by the relative ratio of tidal versus observed current variances, ranged from 18% to 40%.

Surface tidal currents were more energetic than those at 4-m depth except for the M_2 component at EC4 (Table 4). However, these M_2 current differences were

less than 1 cm s^{-1} at both NA2 and EC4. By contrast, the differences in the u component increased to more than 1.5 cm s^{-1} for the K_1 constituent at EC4. Vertical variations with depth suggest that the K_1 tidal currents contained more baroclinic structure than the M_2 constituent, which has a more barotropic component (i.e., phases and amplitudes indicate little vertical variation). The v -component tidal currents explained more of the near-bottom current variations than on the surface at both moorings. For the u component, the tides explained 25%–38% of the observed variance.

At the NA2 mooring, tidal current time series for just the M_2 and K_1 constituents are shown in Fig. 16. The M_2 surface current reflects the variability of the depth-averaged current in both components. That is, the depth-integrated values range between $\pm 4 \text{ cm s}^{-1}$ at the mooring. After removing the depth-independent currents in both velocity components, there is little evidence of baroclinic signature in the M_2 tidal constituent compared to the K_1 tidal current component. The surface K_1 tidal components range between 2 to 2.5 cm s^{-1} compared to a depth-independent values of $\pm 1 \text{ cm s}^{-1}$ for both u and v components (Figs. 16b,d). Surface and depth-integrated currents are also out of phase. Removing this depth-averaged component indicates baroclinic current structure of $\approx 2 \text{ cm s}^{-1}$ in the diurnal component. Thus, the M_2 tidal current has a large barotropic component, whereas the K_1 contains more

TABLE 4. Amplitudes (u, v) and relative phases (ϕ_u, ϕ_v) of diurnal (K_1) and semidiurnal (M_2) tidal components derived from a harmonic analysis of the WERA surface currents ($z = 0$) and the 4-m and near-bottom ADCP current measurements during the WFS experiment over the 33-day time series at NA2 and EC4 moorings. Observed (σ_o^2) and predicted variance (σ_p^2) and variance explained (%) are based on the K_1 and M_2 tidal constituents.

Depth m	K_1				M_2				u			v		
	u cm s ⁻¹	ϕ_u°	v cm s ⁻¹	ϕ_v°	u cm s ⁻¹	ϕ_u°	v cm s ⁻¹	ϕ_v°	σ_o^2	σ_p^2	%	σ_o^2	σ_p^2	%
NA2														
0	2.6	252	2.75	139	4.4	48	3.4	343	62	19	32	121	14	12
4	1.5	225	1.5	141	3.5	28	2.5	323	28	11	38	62	5	8
22	0.8	344	1.3	287	3.7	16	2.4	315	35	9	25	24	5	23
EC4														
0	3.1	246	2.4	121	4.1	51	3.4	352	52	17	33	123	14	12
4	1.4	254	2.3	120	4.4	60	3.3	356	47	16	34	107	16	15
17	2.0	354	1.4	304	4.6	49	3.9	346	55	18	33	38	14	36

baroclinic structure. This result is consistent with previous WFS studies (He and Weisberg 2002a).

b. Effects of wind forcing

Low-pass-filtered surface friction velocity (u_*) and the difference between the wind stress and detided sur-

face current ($\Delta\theta$) directions at NA2 mooring are shown in Fig. 17. Over the 33-day time series, u_* ranged between 0.05 and 0.35 m s⁻¹ during Tropical Storm Henri. The mean u_* was 0.2 m s⁻¹ with a standard deviation of ± 0.06 m s⁻¹. The difference between the wind (and stress) direction and surface current ranged between

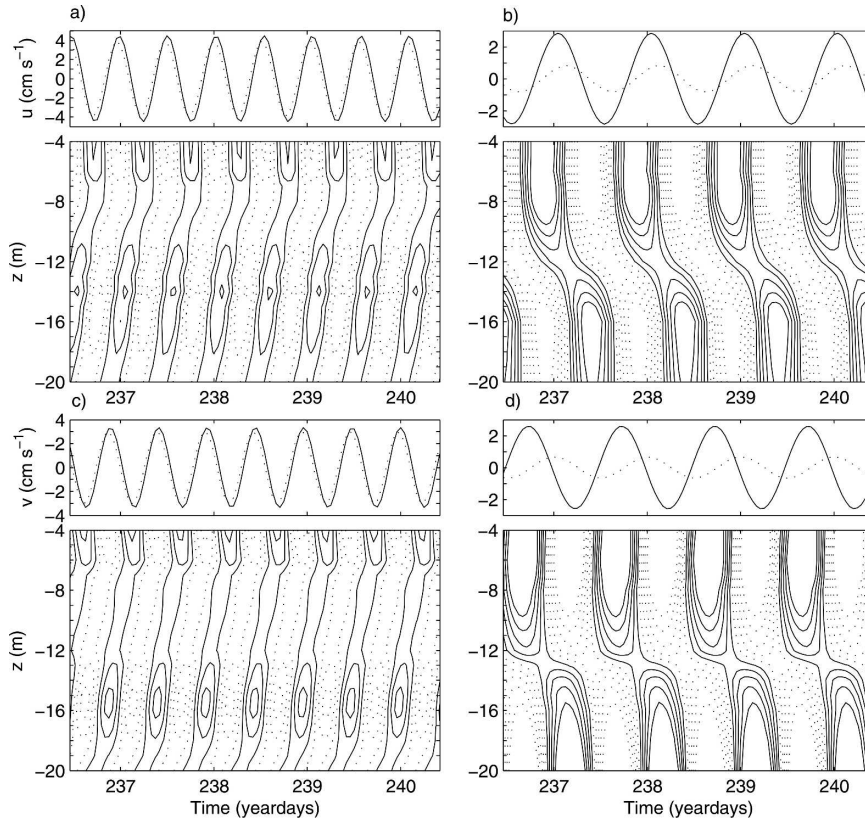


FIG. 16. (left) M_2 and (right) K_1 tidal currents (cm s⁻¹) at the NA2 mooring for the (a), (b) u and (c), (d) v components comparing (top) surface (solid) and depth-integrated ADCP (dashed) tidal currents and (bottom) vertical structure oscillations (observed depth averaged) from 4 to 20 m, contoured at 0.25 cm s⁻¹ intervals.

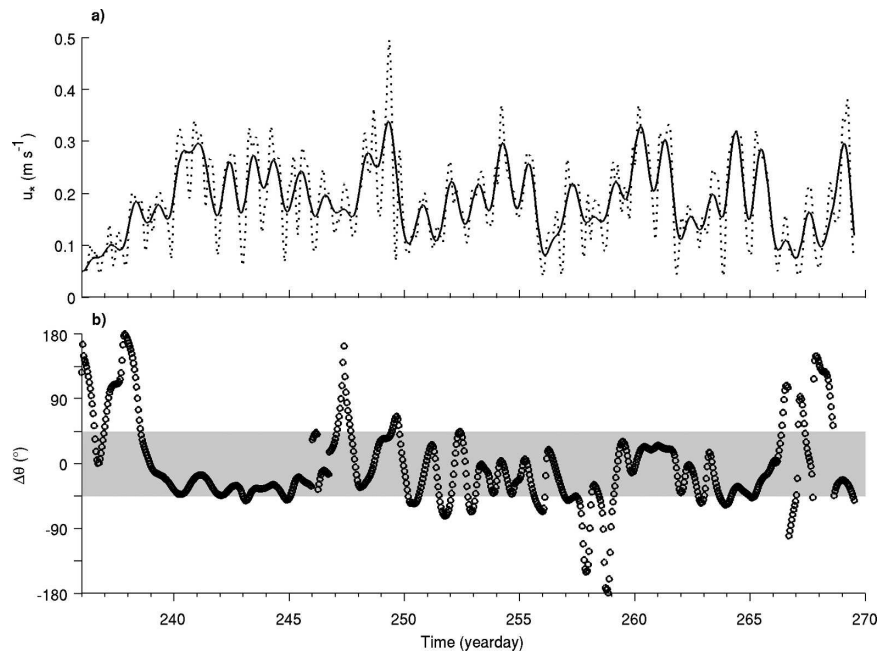


FIG. 17. Time series of low-pass-filtered (solid) (a) surface friction velocity (u_* ; m s^{-1}) and (b) direction difference between the wind stress and surface current direction ($^\circ$) at NA2. In (a) unfiltered u_* is given as the dotted curve. Gray area depicts $\pm 45^\circ$ where a negative difference implies surface currents to the right of the wind stress.

$\pm 180^\circ$ with more than 60% of the differences lying between $\pm 45^\circ$ with an average directional difference of -12° . That is, the mean directional difference is to the right of the wind and stress directions. Notice that these differences were the largest when the surface friction (i.e., wind stress) was the weakest. This mean value is considerably less than predicted by steady-state Ekman dynamics where the time-averaged surface velocity is at an angle of 45° to the right of the stress and are rarely observed in field measurements. However, there is a significant wind-induced current contained in the low-

frequency surface current signals as found by Liu et al. (2007).

To examine these relationships between 10-m surface winds and currents, these data were regressed to determine the bias and slope (Fig. 18). In the east–west direction, regression slope was 0.02 with a bias of -0.9 cm s^{-1} whereas in the north–south direction, the slope was 0.03 with a bias of 1.1 cm s^{-1} . For a surface drift current, the theoretical slope is predicted to be 0.036 or 3.6% (Bye 1967) of the wind speed due to the square root of the ratio of air and water densities. As this

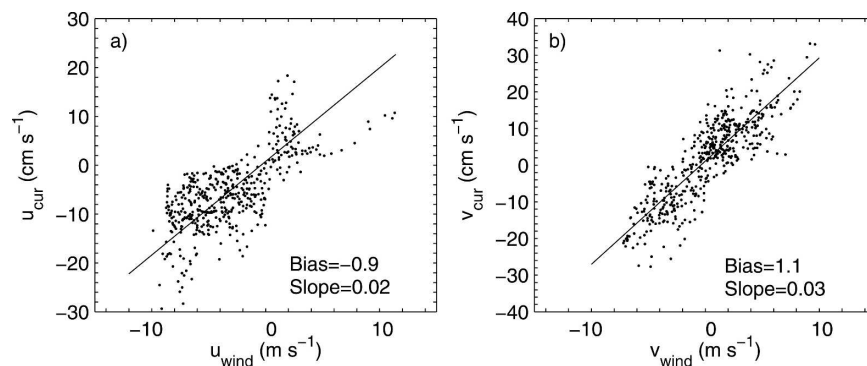


FIG. 18. Regression analysis between wind (m s^{-1}) and detided currents (cm s^{-1}) for (a) u component and (b) v component with the biases and slopes based on Fig. 17 where directional differences between wind and current of $\pm 45^\circ$ ($N = 476$ points $\approx 60\%$ of the data series).

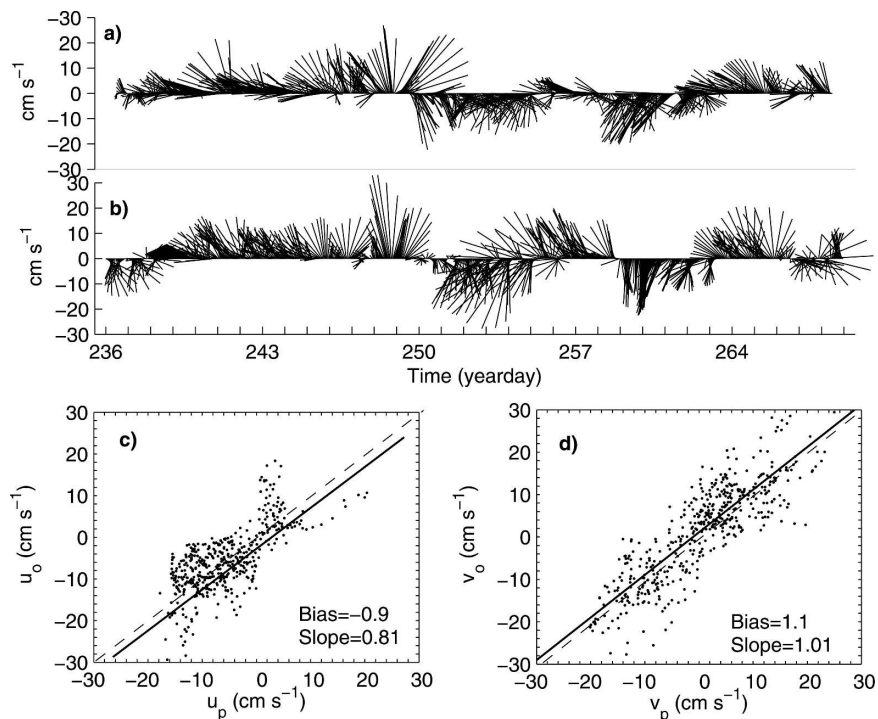


FIG. 19. Comparison between (a) predicted wind-drift current vector based on Fig. 18 and (b) detided current vectors and regression analyses for the (c) u component and (d) v component between predicted (p) and observed (o) detided surface currents (cm s^{-1}) with biases and slopes.

wind-drift flow is assumed to be irrotational, there is also a logarithmic vertical dependence but is not explored here given the 4-m separation between the surface and subsurface measurements. Using upward-looking ADCP profiles to 2 m from an autonomous underwater vehicle (AUV), Shay et al. (2003) found a log-layer representation in the downwind directions. Furthermore, rotating detided surface currents into the wind stress direction following Drennan and Shay (2005) did not reveal any further insights, presumably due to the weaker mean currents than observed over the east Florida shelf.

These slopes and biases are used to construct a time-dependent wind-drift time series as shown in Fig. 19. The predicted time series associated with the wind drift closely follows the detided surface current signals, which suggests the importance of the time-dependent surface winds. This wind component includes the diurnal cycling and longer period or synoptic fluctuations. In some cases, the wind-driven component overpredicts the surface current; however, over most of the time series, there seems to be fairly good agreement. Variance estimates for the wind-driven surface currents are approximately 19 to 21 $\text{cm}^2 \text{s}^{-2}$ in both directions. These results are regressed to examine differences be-

tween the predicted and observed wind-driven currents (Figs. 19c,d). In the east–west direction, the slope is 0.81 with a bias of -0.9 cm s^{-1} . The difference in the predicted and observed surface current indicates a normal distribution centered between -2 and 0 cm s^{-1} . In the north–south direction, there appears to be a slightly better comparison as the slope is $O(1)$ with a bias of 1 cm s^{-1} . However, the wind-drift surface current explains about 50% of the detided current variance in the east–west direction and only 20% of the variance in the north–south current component.

6. Summary and concluding remarks

A dual-station high-frequency WERA, transmitting at 16.045 MHz, was deployed along the WFS during the summer of 2003 overlooking a cross-shelf array of ADCPs (Weisberg et al. 2002). WERA-derived surface currents agreed with 4-m currents measured at these moored ADCPs. Given WERA's performance even during Henri, this radar technology has matured to a point where a coordinated engineering and scientific approach can be used to monitor ocean processes for coastal ocean observing systems (Seim et al. 2003).

A nearly continuous, 33-day vector surface current

time series was acquired starting on 23 August and ending 25 September 2003. In a 16-element phased array mode, WERA mapped coastal ocean currents over a 40 km \times 80 km domain with a horizontal resolution of 1.2 km at \approx 2820 cells. A total of 1628 half-hour snapshots of the two-dimensional current vectors were acquired during this time series, and of these samples, only 70 samples were missing from the vector time series. Complex surface circulation patterns were observed that included tidal currents and an along-shelf current response to Tropical Storm Henri on 5 September 2003. Cyclonically rotating surface winds, adjusted to 10 m in the HF radar domain forced surface velocities of more than 35 cm s⁻¹ as Henri made landfall north of Tampa Bay.

Radial and vector comparisons to subsurface measurements at 4 m from moored ADCPs revealed RMS differences of 4 to 6 cm s⁻¹. Regression analyses indicated slopes close to unity with biases ranging from -2 and 1.6 cm s⁻¹ between surface and subsurface measurements in both current components, respectively. Tidal current amplitudes were 4 to 5 cm s⁻¹ for the M_2 constituents and about 3 to 4 cm s⁻¹ for the K_1 constituent. Vertical structure of the M_2 tidal current indicated that the semidiurnal components were predominantly barotropic with amplitudes exceeding 4 cm s⁻¹ (He and Weisberg 2002a). Diurnal tidal constituents were more baroclinic with a depth-averaged current of about 1 cm s⁻¹. After removal of the tidal components, time-dependent wind-drift currents explained between 20% and 50% in the north-south and east-west directions, respectively. Despite the narrow dynamic range of currents over the WFS, results suggest that the WERA measured the surface velocity well under weak to moderate wind conditions including during Tropical Storm Henri's passage. Clearly, WERA technology can be used to address a broad spectrum of societal needs with respect to coastal surface current monitoring.

Acknowledgments. The authors gratefully acknowledge the support by the ONR through the SEA-COOS program (N00014-02-1-0972) administered by the University of North Carolina at Chapel Hill. The NOAA ACT program provided partial travel support for the WERA deployment personnel. We thank John Lane, Pat Wilson, William Quigley, Larry Heath, Nancy Woodley, and Alan Bullock from the city of Venice for providing the real estate and electricity for our two-month deployment. George Tague, Phil Talley, Jay Moles, Charlie Hunsicker, Karen Windom, and Robert Brown from Manatee County provided access to Coquina Beach. Suzi Fox of the Turtle Watch Education Center approved the deployment. The Department of

Environmental Protection (Renate Skinner, Steve West) permitted us to use the sites. We also thank Thomas Helzel for his assistance in deploying the radar for this acceptance test and Klaus-Werner Gurgel for assistance in using the software and in particular the radial current accuracy algorithm. We thank Larry Kanitz and Dave Powell for logistical support, and the support of Dean Otis Brown is appreciated. Finally, we thank the reviewers for their insightful comments and the patience of the Chief Editorial Office.

REFERENCES

- Balsley, B. B., A. C. Riddle, W. L. Ecklund, and D. A. Carter, 1987: Sea surface currents in the equatorial Pacific from VHF radar backscatter observations. *J. Atmos. Oceanic Technol.*, **4**, 530-535.
- Barrick, D. E., 1992: First order theory and analysis of MF/HF/VHF scatter from the sea. *IEEE Trans. Antennas Propag.*, **AP-20**, 2-10.
- Broche, P., J. C. Crochet, J. L. de Maistre, and P. Forget, 1987: VHF radar for ocean surface current and sea state remote sensing. *Radio Sci.*, **22**, 69-75.
- Bye, J. A., 1967: The wave-drift current. *J. Mar. Res.*, **25** (1), 95-102.
- Chapman, R. D., L. K. Shay, H. C. Graber, J. B. Edson, A. Karachintsev, C. L. Trump, and D. B. Ross, 1997: On the accuracy of HF radar surface current measurements: Inter-comparisons with ship-based sensors. *J. Geophys. Res.*, **102**, 18 737-18 748.
- Crombie, D. D., 1955: Doppler spectrum of sea echo at 13.56 M.c.s⁻¹. *Nature*, **175**, 681-682.
- Drennan, W., and L. K. Shay, 2005: On the variability of the fluxes of momentum and sensible heat. *Bound.-Layer. Meteor.*, **119**, 81-107.
- Emery, B. M., L. Washburn, and J. Harlan, 2004: Evaluating radial current measurements from CODAR high-frequency radar with moored current measurements. *J. Atmos. Oceanic Technol.*, **21**, 1259-1271.
- Essen, H. H., K. W. Gurgel, and T. Schick, 2000: On the accuracy of current measurements by means of HF radar. *IEEE J. Oceanic Eng.*, **25**, 472-480.
- Fairall, C., E. F. Bradley, D. P. Rogers, J. B. Edson, and G. S. Young, 1996: Bulk parameterization of air-sea fluxes for the Tropical Ocean Global Atmosphere Coupled Ocean-Atmosphere Response Experiment. *J. Geophys. Res.*, **101** (C2), 3747-3764.
- Foreman, M. G., 1981: Manual for tidal height analysis and prediction. Tech. Rep. Pacific Marine Science 77-10, Institute of Ocean Science, Victoria, BC, Canada, 97 pp.
- Graber, H. C., B. K. Haus, R. D. Chapman, and L. K. Shay, 1997: HF radar comparisons with moored estimates of current speed and direction: Expected differences and implications. *J. Geophys. Res.*, **102**, 18 749-18 766.
- Gurgel, K.-W., G. Antonischki, H.-H. Essen, and T. Schlick, 1999a: Wellen Radar (WERA): A new ground wave HF radar for remote sensing. *Coastal Eng.*, **37**, 219-234.
- , H.-H. Essen, and S. P. Kingsley, 1999b: High frequency radars: Limitations and recent developments. *Coastal Eng.*, **37**, 201-218.
- Haus, B. K., J. Wang, J. Rivera, N. Smith, and J. Martinez-

- Pedraja, 2000: Remote radar measurements of shelf currents off Key Largo. *Estuarine Coast. Shelf Sci.*, **51**, 553–569.
- He, R., and R. H. Weisberg, 2002a: Tides on the west Florida shelf. *J. Phys. Oceanogr.*, **32**, 3455–3473.
- , and —, 2002b: West Florida shelf circulation and temperature budget for the 1999 spring transition. *Cont. Shelf Res.*, **22**, 719–748.
- , and —, 2003: A Loop Current intrusion case study on the West Florida Shelf. *J. Phys. Oceanogr.*, **33**, 465–477.
- Kundu, P. K., 1976: Ekman veering observed near the ocean bottom. *J. Phys. Oceanogr.*, **6**, 238–242.
- Li, Z., and R. H. Weisberg, 1999: West Florida shelf response to upwelling favorable winds: Kinematics. *J. Geophys. Res.*, **104**, 13 507–13 527.
- Liu, Y., R. H. Weisberg, and L. K. Shay, 2007: Current patterns on the west Florida Shelf from joint self-organizing map analyses of HF radar and ADCP data. *J. Atmos. Oceanic Technol.*, in press.
- Lipa, B. J., and D. E. Barrick, 1983: Least-squares methods for the extraction of surface currents from CODAR crossed loop data: Application at ARSLOE. *IEEE J. Ocean Eng.*, **8** (4), 226–253.
- Marmorino, G. W., C. Y. Shen, C. L. Trump, N. Allan, F. Askari, D. B. Trizna, and L. K. Shay, 1998: An occluded coastal ocean front. *J. Geophys. Res.*, **103**, 21 587–21 600.
- Martinez-Pedraja, J., L. K. Shay, T. M. Cook, and B. K. Haus, 2004: Technical Report: Very-high frequency surface current measurement along the inshore boundary of the Florida Current during NRL 2001. RSMAS Tech. Rep. 2004–03, Rosenstiel School of Marine and Atmospheric Sciences, University of Miami, 34 pp.
- Paduan, J. D., and L. K. Rosenfeld, 1996: Remotely sensed surface currents in Monterey Bay from shore-based HF radar (Coastal Ocean Dynamics Application Radar). *J. Geophys. Res.*, **101**, 20 669–20 686.
- Peters, H., L. K. Shay, A. J. Mariano, and T. M. Cook, 2002: Current observations over a narrow shelf with large ambient vorticity. *J. Geophys. Res.*, **107**, 3087, doi:10.1029/2001JC000813.
- Prandle, D., 1987: The fine-structure of nearshore tidal and residual circulations revealed by HF radar surface current measurements. *J. Phys. Oceanogr.*, **17**, 231–245.
- Seim, H., and Coauthors, 2003: SEA-COOS—A model for multi-state, multi-institution regional observation system. *MTS J.*, **37** (3), 92–101.
- Shay, L. K., H. C. Graber, D. B. Ross, and R. D. Chapman, 1995: Mesoscale ocean surface current structure detected by HF radar. *J. Atmos. Oceanic Technol.*, **12**, 881–900.
- , S. J. Lentz, H. C. Graber, and B. K. Haus, 1998a: Current structure variations detected by high frequency radar and vector measuring current meters. *J. Atmos. Oceanic Technol.*, **15**, 237–256.
- , T. N. Lee, E. J. Williams, H. C. Graber, and C. G. H. Rooth, 1998b: Effects of low frequency current variability on submesoscale near-inertial vortices. *J. Geophys. Res.*, **103**, 18 691–18 714.
- , T. M. Cook, Z. Hallock, B. K. Haus, H. C. Graber, and J. Martinez, 2001: The strength of the M_2 tide at the Chesapeake Bay mouth. *J. Phys. Oceanogr.*, **31**, 427–449.
- , and Coauthors, 2002: Very high-frequency radar mapping of surface currents. *IEEE J. Oceanic Eng.*, **27** (2), 155–169.
- , T. M. Cook, and P. E. An, 2003: Submesoscale coastal ocean flows detected by very high frequency radar and autonomous underwater vehicles. *J. Atmos. Oceanic Technol.*, **20**, 1583–1600.
- Stewart, R. H., and J. W. Joy, 1974: HF radio measurements of surface currents. *Deep-Sea Res.*, **21**, 1039–1049.
- Teague, C. A., J. F. Vesecky, and Z. R. Hallock, 2001: A comparison of multifrequency HF radar and ADCP measurements of near-surface currents during Cope-3. *IEEE J. Oceanic Eng.*, **26**, 399–405.
- Weisberg, R. H., and R. He, 2003: Local and deep-ocean forcing contributions to anomalous water properties on the West Florida Shelf. *J. Geophys. Res.*, **108**, 3184, doi:10.1029/2002JC001407.
- , —, M. Luther, J. Walsh, R. Cole, J. Donovan, C. Mertz, and V. Subramanian, 2002: A coastal ocean observing system and modeling program for the west Florida Shelf. *Proc. MTS/IEEE Oceans 2002 Conf.*, Biloxi, MS, IEEE, 530–534.
- Weller, R., and R. E. Davis, 1980: A vector measuring current meter. *Deep-Sea Res.*, **27**, 575–582.
- Yang, H., and R. H. Weisberg, 1999: Response of the west Florida shelf circulation to climatological wind stress forcing. *J. Geophys. Res.*, **104**, 5301–5320.